Magnon currents excited by the spin Seebeck effect in ferromagnetic EuS thin films

M. Xochitl Aguilar-Pujol,[1,*] Sara Catalano,[1,*] Carmen González-Orellana,[2] Witold Skowroński,[1,3] Juan M. Gomez-Perez,[1] Maxim Ilyn,[2] Celia Rogero,[2,4] Marco Gobbi,[1,2,5] Luis E. Hueso,[1,5] and Fèlix Casanova[1,5,†]

[1]*CIC NanoGUNE BRTA, 20018 Donostia-San Sebastian, Basque Country, Spain*

[2]*Centro de Física de Materiales CSIC-UPV/EHU, 20018 Donostia-San Sebastian, Basque Country, Spain*

[3]*AGH University of Krakow, Institute of Electronics, 30-059 Krakow, Poland*

[4]*Donostia International Physics Center (DIPC), 20018 Donostia-San Sebastian, Basque Country, Spain*

[5]*IKERBASQUE, Basque Foundation for Science, 48009 Bilbao, Basque Country, Spain*

(Received 21 August 2023; revised 9 November 2023; accepted 13 November 2023; published 14 December 2023)

A magnetic insulator is an ideal platform to propagate spin information by exploiting magnon currents. However, until now, most studies have focused on $Y_3Fe_5O_{12}$ (YIG) and a few other ferri- and antiferromagnetic insulators, but not on pure ferromagnets. In this study, we demonstrate that magnon currents can propagate in ferromagnetic insulating thin films of EuS. By performing both local and nonlocal transport measurements in 18-nm-thick films of EuS using Pt electrodes, we detect magnon currents arising from thermal generation by the spin Seebeck effect. By comparing the dependence of the local and nonlocal signals with the temperature ($<$30 K) and magnetic field ($<$9 T), we confirm the magnon transport origin of the nonlocal signal. Finally, we extract the magnon diffusion length in the EuS film ($\sim$140 nm), a short value in good correspondence with the large Gilbert damping measured in the same film.

DOI: 10.1103/PhysRevB.108.224420

I. INTRODUCTION

Magnons, the collective bosonic excitations in magnetically ordered systems, can propagate and transport spin angular momentum even in insulators [1,2]. However, to pave the way for pure spin-based information, spin signals in magnetic insulators must integrate with conventional electronics [1]. Therefore, the ideal platform for these devices comprises the interface between a metal and a magnetic insulator. This arrangement enables the transport of spin angular momentum between the electrons of the metal and the magnons in the magnetic insulator via the interfacial exchange interaction, which is quantified by the spin-mixing conductance. Incoherent magnon currents can be excited both electrically, by means of the spin Hall effect (SHE), or thermally, due to the spin Seebeck effect (SSE) [1–3]. In order to detect these magnon currents, the inverse spin Hall effect (ISHE) can be used, since it transforms back a spin current into a charge current, enabling all-electrical access to spin current physics [2,3].

So far, magnon transport in magnetic insulators has been studied mainly through ferrimagnetic garnets with the prototypical example being $Y_3Fe_5O_{12}$ (YIG), whose exceptionally small Gilbert damping results in a magnon diffusion length of several microns [4–6]. Magnon transport has also been reported in some antiferromagnetic insulators, showing characteristic magnon diffusion lengths of a few hundreds of nm [7,8]. Indeed, there is increasing interest in extending the knowledge of magnon transport to other magnetic compounds. For example, recent studies have focused on magnon excitations in van der Waals magnetic insulators [9–12]. In this context, spin Hall magnetoresistance (SMR) measurements on Eu-based insulating ferromagnets have recently demonstrated intriguing spin-transport properties at the interface with heavy metal films, suggesting that they could also be employed as carriers of magnon spin currents [13–15].

Europium sulphide (EuS), one of the few examples of an isotropic Heisenberg ferromagnetic insulator [16,17], can be grown as thin films exhibiting the ferromagnetic ground state below the Curie temperature $T_C \approx 18$ K, which can be tuned by chemical doping or strain [18]. Below T_C, it behaves as a soft ferromagnet with extremely small coercive fields, similar to YIG. EuS films have been used to introduce strong magnetic exchange fields within interfacial layers such as metals, superconductors, and topological insulators, and manipulate their electronic phases by the magnetic proximity effect [15,19–30]. Specifically, EuS/Pt interfaces have recently been studied by means of SMR measurements, revealing a strong exchange field into the heavy metal layer, even for polycrystalline EuS films [15].

In this paper, we demonstrate the propagation of magnon spin currents in a ferromagnetic insulating thin film of EuS. Pt nanostructures were used to generate and detect magnon currents through evaporated polycrystalline EuS films. Below the T_C of EuS, we show that magnon currents generated by the SSE at the Pt/EuS interface can propagate through the EuS films. We study such an effect by electrically detecting the magnon currents at the Pt/EuS interface considering both the local and the nonlocal configuration. We also explore the temperature, magnetic field, and length dependence of the signal, which indicate that thermally induced magnon currents

*These authors contributed equally to this work.
†f.casanova@nanogune.eu

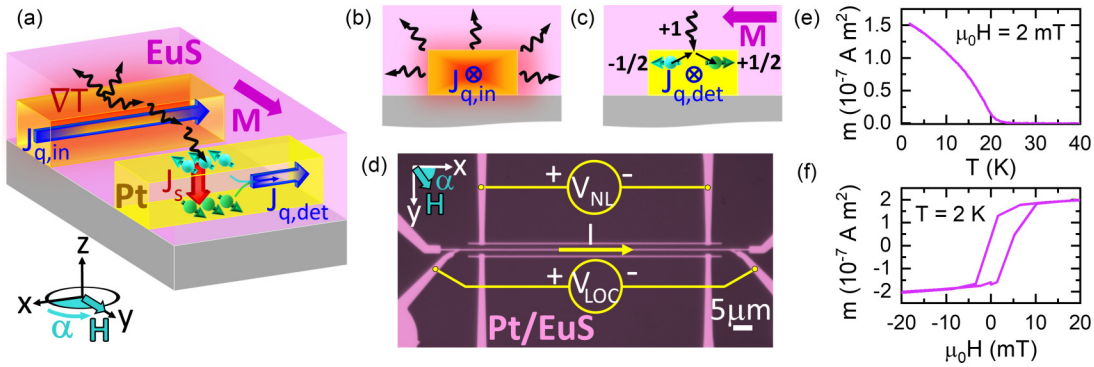

FIG. 1. (a) Schematic representation of the physical processes that occur in the Pyrex/Pt/EuS system. Two Pt strips are embedded in the magnetic insulator (EuS) with magnetization M following the in-plane magnetic field H applied, which can rotate an angle α in the sample plane. When a charge current density $J_{q,\mathrm{in}}$ is applied through the left Pt strip, a radial thermal gradient ΔT appears due to Joule heating, generating nonequilibrium magnons (black arrows) that diffuse away. This leads to a magnon accumulation at the second Pt strip that interacts with the electron spins of the heavy metal creating a spin accumulation that induces a spin current density J_s. Due to the ISHE, J_s is transformed into a charge current density $J_{q,\mathrm{det}}$, that can be electrically detected. (b) The applied $J_{q,\mathrm{in}}$, generates a thermal gradient due to Ohmic losses that gives rise to a magnon flow away from the injector. (c) Spin-flip scattering process leading to a transfer of spin angular momentum between the Pt electrons and the EuS magnons at the Pt/EuS interface. (d) Optical microscope image of a device, showing the measurement configuration where I denotes the charge current applied, and V_{LOC}, V_{NL} are the local and nonlocal voltages measured, respectively. (e) Temperature dependence of the magnetic moment measured at a magnetic field of 2 mT in the Pyrex/Pt/EuS sample. (f) Magnetic hysteresis loop measured in the Pyrex/Pt/EuS sample at 2 K, with a step size of 2.5 mT.

propagate in the diffusive transport regime in our samples. We extract a thermal magnon diffusion length ℓ_m^{th} of $\sim$140 nm, much smaller than the one observed in YIG, suggesting that magnons are strongly damped in the studied EuS films, in good correspondence with the measured Gilbert damping α_{G} ($\sim$0.04). Our work further expands the present knowledge of magnon transport to a broader class of materials.

II. EXPERIMENTAL DETAILS

Pt/EuS heterostructures have been fabricated on top of insulating Pyrex substrates, following the procedure presented in our previous work [15]. First, 5 nm of Pt were deposited with DC magnetron sputtering on top of the Pyrex substrate [31]. Subsequently, the magnon spin transport (MST) devices were defined by *e*-beam lithography and Ar-ion milling. Each MST device consists of two or three Pt strips (width of 300 nm and length of 70 μm) separated by different distances d(0.8 μm $< d <$ 2 μm). Afterwards, 18 nm of EuS were evaporated *ex situ* on top of the Pt contacts, with the same deposition method reported by Gomez-Perez *et al.* [15]. Since the top surface of the EuS film oxidizes when it is exposed to air, the final film corresponds to around 14 nm of insulating EuS capped by $\sim$4 nm of EuO_x, which is also insulating [32]. An optical image of a representative device is shown in Fig. 1(d).

Transport measurements were carried out using a Quantum Design physical property measurement system (PPMS) covering the temperature range 2 K $< T <$ 300 K. We applied magnetic fields H up to $\mu_0 H = 9$ T and the sample was rotated in the xy plane [α plane, inset of Fig. 1(a)]. We applied a DC current I in the range 4 μA $< I <$ 100 μA with a Keithley 6221 current source meter and measured the voltage with a Keithley 2182 nanovoltmeter. As sketched in Fig. 1(d), I is applied through one Pt strip, and we studied the voltage response in two configurations. We either detect the voltage along the same strip, which we refer to as local voltage V_{LOC}, or we detect it in a second Pt strip separated by a distance d, that we denote as a nonlocal voltage V_{NL}. We analyzed the first and second harmonic components of the detected voltages V_{LOC} and V_{NL} by applying the DC current reversal technique [33,34]. We extracted the first harmonic or electrical response component from $V^e_{\mathrm{LOC,NL}} = [V_{\mathrm{LOC,NL}}(I+) - V_{\mathrm{LOC,NL}}(I-)]/2$. The second harmonic component, or thermal voltage response, is provided by $V^{\mathrm{th}}_{\mathrm{LOC,NL}} = [V_{\mathrm{LOC,NL}}(I+) + V_{\mathrm{LOC,NL}}(I-)]/2$ [4,33–35].

The magnetic properties of the EuS film have been measured with the vibrating sample magnetometer (VSM) and ferromagnetic resonance (FMR) options of the Quantum Design PPMS.

III. RESULTS AND DISCUSSION

We studied the generation and transport of spin angular momentum in EuS films by incoherent magnon currents, which can be driven by nonequilibrium magnon density and temperature gradients [36]. In fact, a magnon spin current j_m can propagate in a magnetic medium according to the equation

$$\frac{2e}{\hbar} j_m = \left(-\sigma_m \nabla \mu_m + \frac{L}{T} \nabla T_m \right),$$

where σ_m is the magnon spin conductivity, μ_m is the nonequilibrium magnon chemical potential, L is the spin Seebeck coefficient of the medium, T is the average equilibrium temperature of the magnon bath, and ∇T_m is the temperature gradient applied to the system [37].

In our experiment, we adopted the same measurement configuration used by Cornelissen *et al.* [4]. As sketched in Fig. 1(d), a charge current I is applied through a metallic Pt strip (injector) and the voltage response is measured along the

same strip ($V_{\rm LOC}$) or at a different strip ($V_{\rm NL}$). We recorded both the first ($V^e_{\rm LOC}$, $V^e_{\rm NL}$) and second harmonic ($V^{\rm th}_{\rm LOC}$, $V^{\rm th}_{\rm NL}$) response with the DC current reversal technique [33,34], as described in Sec. II.

The measurements principle is illustrated in Fig. 1(a). The applied I along the x axis of the Pt wire corresponds to a charge current density $j_{q,\rm in}$ that generates a spin accumulation polarized along the y axis at the Pt/EuS interface thanks to the SHE. The effects of the interaction between the spin current flowing in the Pt strip in z axis and the interfacial magnetic layer can be read out in the first order, or *electrical*, response of the system as a voltage $V^e_{\rm LOC,NL}$. By measuring $V^e_{\rm LOC}$ we study the SMR effect in our samples, that is the modulation of the Pt resistance due to the torque exerted by the magnetization ($\boldsymbol{M}$) of the EuS on the spin current flowing through Pt [38,39]. Moreover, the spin current can also generate magnons at the Pt/EuS interface by spin-flip scattering processes, as sketched in Fig. 1(c). Furthermore, when the magnons diffuse away and reach a second Pt strip, they can transfer spin angular momentum to the Pt electrons due to the same spin-flip scattering process [Fig. 1(c)]. This produces a spin current through the Pt/EuS interface and, consequently, a voltage in the Pt wire, due to the ISHE. Thus, the electrically injected magnon currents are detected as $V^e_{\rm NL}$ in the second Pt wire.

Most important for our work, the applied $j_{q,\rm in}$ also generates Joule heating at the Pt/EuS interface, so that a temperature gradient proportional to the square of the current (I^2) is introduced in the system [Fig. 1(b)]. The second order, or *thermal*, response of the system to such a gradient is detected as $V^{\rm th}_{\rm LOC,NL}$. When the thermal gradient appears, the magnon population is driven out of equilibrium and a magnon current can flow between the hot and the cold side of the system [black arrows in Figs. 1(a)–1(c)], resulting in the SSE. At the interface with the Pt wire, the magnon spin angular momentum is transferred to the Pt electrons through spin-flip scattering processes [Fig. 1(c)], yielding a thermal voltage response $V^{\rm th}_{\rm LOC,NL}$. We note here that the thermal voltage due to the SSE can be detected both locally ($V^{\rm th}_{\rm LOC}$) and nonlocally ($V^{\rm th}_{\rm NL}$), as thermally induced magnon currents [black arrows in Figs. 1(a)–1(c)] diffuse through the EuS film [1,40,41].

The geometry of the experiment allows the SMR and magnon-induced voltages to be probed through the Pt wires. We take into account that both phenomena depend on the orientation between the spin polarization $\boldsymbol{s}$ of the electrons in the Pt (fixed along the y axis) and $\boldsymbol{M}$ of EuS. For that reason, we saturate $\boldsymbol{M}$ in the plane of the film (xy plane) with an external magnetic field H [inset of Fig. 1(a)], and we rotate it. Thus, since the generated spin current is absorbed by $\boldsymbol{M}$ as a spin-transfer torque if $\boldsymbol{M} \perp \boldsymbol{s}$, SMR results in a $\cos^2\alpha$ angular dependence when $\boldsymbol{M}$ of the EuS film is rotated in plane [Fig. 1(a)] [42]. However, spin-flip scattering processes depend on the scalar product between $\boldsymbol{M}$ and $\boldsymbol{s}$, causing the electrically injected and detected magnon currents to exhibit a $\sin^2\alpha$ dependence [4]. Finally, since spin flip only occurs at the detector for the thermal injection, it results in a $\sin\alpha$ dependence [4].

The magnetic properties of the studied EuS film are exemplified in Figs. 1(e) and 1(f), which present the total magnetic moment (m) of the sample as a function of temperature and applied magnetic field, respectively. As shown in Fig. 1(e), EuS exhibits a clear ferromagnetic behavior with a $T_{\rm C} \approx 19$ K, in agreement with previous reports [15,18]. The hysteresis loop at 2 K in Fig. 1(f), with a coercive field around 3 mT, confirms the ferromagnetic behavior of the EuS film (see Sec. S5 of the Supplemental Material [43] for more details) [15].

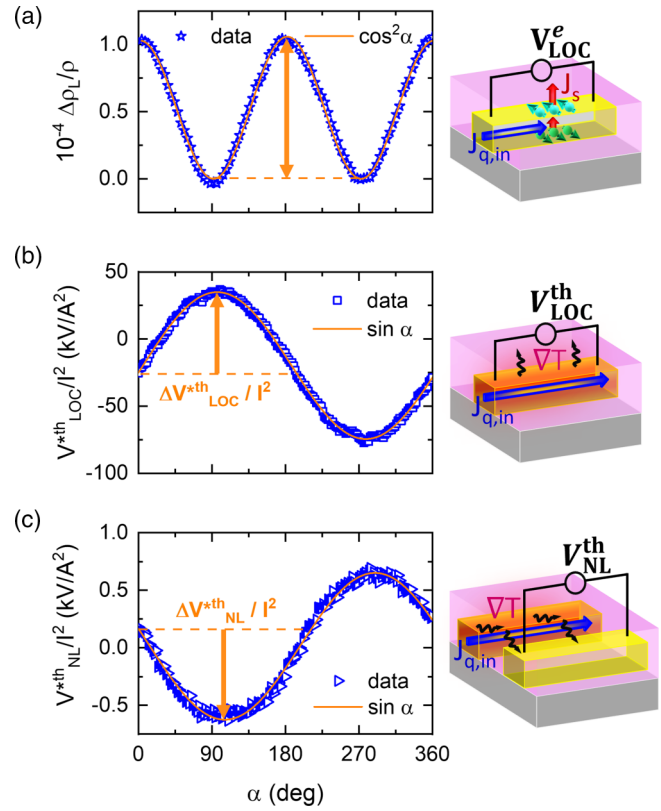

FIG. 2. Representative (a) ADMR of the SMR at a fixed magnetic field of $\mu_0 H = 0.1$ T. (b) Local SSE and (c) nonlocal SSE at 0.8 μm, both at $\mu_0 H = 0.3$ T, where the voltage is normalized to the square of the applied current. The measurement temperature is 2 K and the current applied is 20 μA. The arrows indicate the amplitude of the signal. A schematic illustration of the effect measured is included on the right side of the corresponding panel. All data correspond to device MST1.

A. Angle dependence of the electrical and thermal response

Figure 2(a) presents the angular-dependent magnetoresistance (ADMR) measured in MST1 as a function of the in-plane angle α, at $T = 2$ K, below $T_{\rm C}$ of EuS. We saturate $\boldsymbol{M}$ in plane by applying a small external field ($\mu_0 H = 0.1$ T). The data are extracted from the electrical local response $V^e_{\rm LOC}$ in order to provide the SMR signal $\Delta\rho_L/\rho = [R_L(\alpha) - R_L(90^\circ)]/R_L(90^\circ)$, where $R_L = V^e_{\rm LOC}/I$ is the longitudinal resistance. We observe a clear $\cos^2\alpha$ modulation of the Pt resistance, as expected for the SMR effect [38,39,47]. The signal amplitude [double arrow in Fig. 2(a)] is of the order of 10^{-4}, consistent with previous results in EuS/Pt interfaces and comparable to the magnitude of the SMR measured in Pt/YIG interfaces [15,47,48]. Field-dependent magnetoresistance (FDMR) measurements confirm the typical magnetic behavior of EuS, displaying the

SMR gap and magnetoresistance peaks in correspondence with the expected magnetization reversal of EuS (see the Supplemental Material [43], Sec. S1). The large SMR amplitude and clear correlation with M of EuS indicate an efficient spin transfer at the EuS/Pt interface, in other words, a favorable spin-mixing conductance [14,15,49]. We note that, from the SMR measurements, we can infer the spin transfer efficiency of each device, which we use to normalize the data to compare the response of different devices, as described in the Supplemental Material [43], Sec. S2. Hereafter, we label the normalized measured voltage V^{*}_{LOC} and V^{*}_{NL}.

Next, we study the magnon currents. For these measurements, a current $I \leqslant 20$ μA is applied through an injector strip as sketched in the right panel of Figs. 2(b) and 2(c). Note that the injected current is chosen to be small in order to keep the local temperature below the Curie point of the EuS film, as verified by measuring the four-point resistance of the Pt injector. A detailed calibration of the injector temperature with respect to the applied current is provided in the Supplemental Material [43], Sec. S2.

First, we measure the thermal local amplitude $V^{*\mathrm{th}}_{\mathrm{LOC}}$ (which we normalize to I^2) as a function of α at $T = 2$ K and $\mu_0 H = 0.3$ T. $V^{*\mathrm{th}}_{\mathrm{LOC}}/I^2$ shows a clear $\sin\alpha$ modulation, as presented in Fig. 2(b) for device MST1. The $\sin\alpha$ angular dependence is consistent with the symmetry expected for the SSE [4]. A constant angle-independent voltage offset is also present due to other thermoelectric effects [4,6,8,50]. Second, we study the propagation of magnon currents through the nonlocal voltage. For the electrically injected magnon currents, that follows a $\sin^2\alpha$ dependence, we found no signal in V^{e}_{NL} (Supplemental Material [43], Sec. S3) at any of the measured distances $0.8\ \mu\mathrm{m} < d < 2\ \mu\mathrm{m}$. In contrast, the $V^{*\mathrm{th}}_{\mathrm{NL}}/I^2$ signal is similar to the local $V^{*\mathrm{th}}_{\mathrm{LOC}}/I^2$ with the same clear $\sin\alpha$ modulation expected for the SSE, but with opposite sign, as shown in Fig. 2(c) for MST1 with $d = 0.8$ μm. The offset signal due to other thermoelectric effects is also present for the nonlocal case. The $\sin\alpha$ angular dependence, verified at all the measured distances for $V^{*\mathrm{th}}_{\mathrm{NL}}/I^2$, is consistent with the symmetry expected for SSE-induced magnon currents [4,34,35]. However, the inverted sign suggests that magnon currents at the injector/detector strips are flowing in opposite directions [Figs. 2(b) and 2(c)]. In fact, such a sign change is expected to occur between the SSE induced magnon currents measured locally and nonlocally, due to the redistribution of the magnon population induced by Joule heating [51–53]. As Joule heating depletes the magnon distribution at the injector site, the magnon currents are expected to flow towards (away from) the detector (the injector) as also illustrated by the direction of the black arrows in Figs. 1(b) and 1(c) [37,51,52]. For all the devices measured, we observed a positive local $V^{*\mathrm{th}}_{\mathrm{LOC}}/I^2$ amplitude and a negative nonlocal $V^{*\mathrm{th}}_{\mathrm{NL}}/I^2$ amplitude.

All things considered, the Pt/EuS devices reveal a magnon-induced response to Joule heating, consistent with the symmetry of the SSE. The absence of an analog signal in the nonlocal electrical response V^{e}_{NL}, in contrast, suggests that the magnon population redistribution induced by the spin-flip scattering process at the injector Pt/EuS interface is too small to produce a measurable signal at the detector. We note here that V^{e}_{NL}/I has been reported to vanish as the temperature is lowered below 50 K in Pt/YIG interfaces by different groups [35,54,55]. Thus, the absence of a signal V^{e}_{NL}/I^2 for our samples is expected in the measured temperature range.

B. Temperature dependence

Subsequently, we analyze the temperature dependence of the SMR, local SSE, and nonlocal SSE amplitudes [defined in Fig. (2)], which are presented in Fig. 3 for devices MST1 and MST3. In all cases, the amplitude of the signal is maximum for the lowest temperature measured (2 K) and decreases with increasing temperature. However, we observe a clear difference between the SMR curve and the thermal amplitudes $V^{*\mathrm{th}}_{\mathrm{LOC}}/I^2$ and $V^{*\mathrm{th}}_{\mathrm{NL}}/I^2$, as can be observed in Fig. 3(d). The temperature dependence of the SMR amplitudes [Fig. 3(a)] follows the expected trend vanishing as the temperature is raised above the Curie point of the EuS film [see Fig. 1(e) and the Supplemental Material [43], Fig. S7]. In fact, we note here that we can measure an SMR signal even above the T_{C} of the EuS films. The presence of such a finite SMR response above T_{C} is a consequence of the sensitivity of the SMR to the magnetic correlations [56], which are present even above T_{C} in our films, according to our VSM characterization (Supplemental Material [43], Sec. S5). The observed temperature dependence of SMR in our EuS thin films can be fully explained in terms of the microscopic theory developed by Zhang *et al.* [15,57]. Instead, the temperature dependence of $V^{*\mathrm{th}}_{\mathrm{LOC}}/I^2$ [Fig. 3(b)] and $V^{*\mathrm{th}}_{\mathrm{NL}}/I^2$ [Fig. 3(c)] show a similar trend with a substantially different decrease from the SMR curve as T_{C} is approached [Fig. 3(d)]. Such a temperature dependence may seem surprising for SSE-induced thermal voltages, for which the SSE theory predicts a linear dependence with the system magnetization [58]. However, a similar behavior has been reported in other experimental studies of the SSE at low temperatures [35,54] and can be qualitatively understood with the following considerations. First, the Joule heating induced temperature gradient is very likely temperature dependent, as the thermal conductivities of Pt, EuS, and the Pyrex substrate may strongly change and at different rates as the temperature is lowered. Second, the Gilbert damping of the EuS film also varies at such temperatures (see the Supplemental Material [43], Fig. S8) due to the very low T_{C} of the films, which consequently affects the propagation of magnon currents. Elaborating a model that captures such temperature dependent effects on the measured thermal voltages is a challenging task, which goes beyond the scope of this work. Instead, we remark that all the measured signals disappear above the T_{C} of the EuS film, confirming the magnetic origin of the studied voltages.

C. Magnetic field dependence

We also examine the magnetic field dependence of the SMR, local SSE, and nonlocal SSE amplitudes, as illustrated in Fig. 4. Initially, both the SMR and SSE signals increase as $\boldsymbol{M}$ of the system develops, since both effects are related to the interaction of the spins of the electrons in Pt with the magnetic moments in the magnetic layer; but as $\boldsymbol{M}$ continues to grow, their behavior diverges. The SMR response tends to saturate with the magnetic field [Fig. 4(a)], in correspondence with the saturation of $\boldsymbol{M}$ in the EuS films. Note here that the saturation

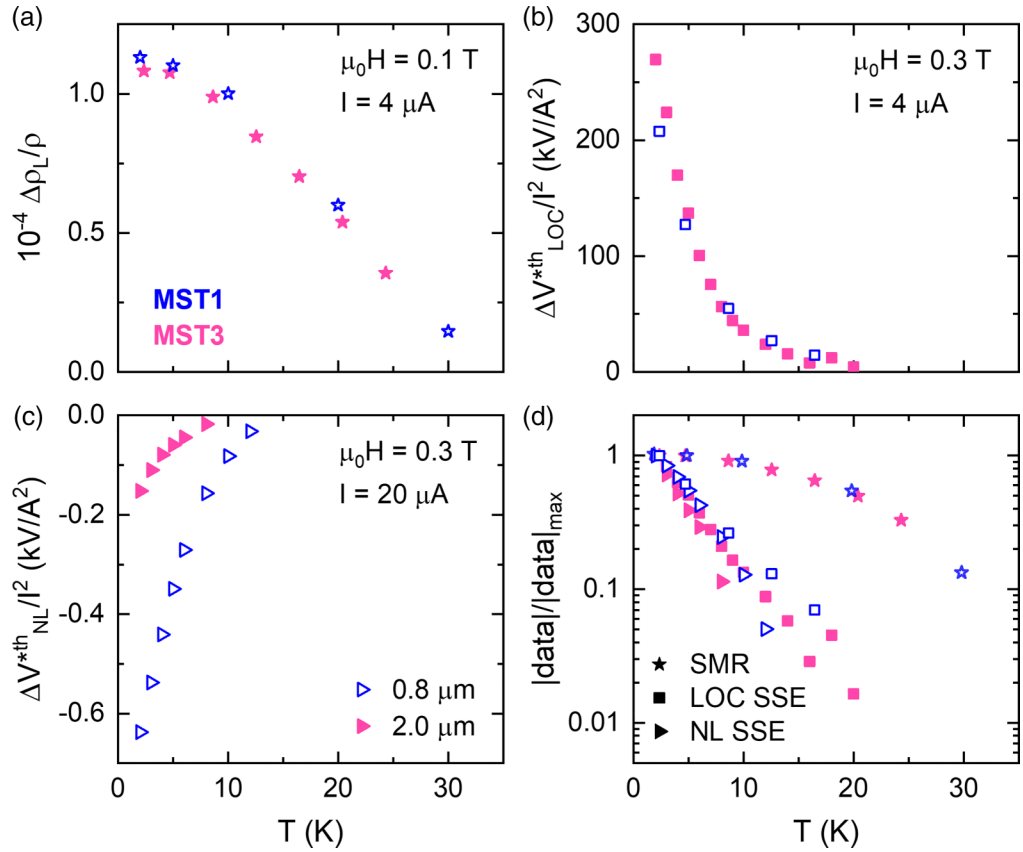

FIG. 3. (a) SMR amplitudes [as defined in Fig. 2(a)] at $\mu_0 H = 0.1$ T and $I = 4$ μA, (b) local SSE amplitudes [as defined in Fig. 2(b)] at $\mu_0 H = 0.3$ T and $I = 4$ μA, and (c) nonlocal SSE amplitudes [as defined in Fig. 2(c)], at $\mu_0 H = 0.3$ T and $I = 20$ μA for two different distances (0.8 and 2.0 μm), as a function of temperature. (d) Comparison of SMR, local SSE, and nonlocal SSE amplitudes normalized to their maximum values. Data correspond to devices MST1 (blue open symbols) and MST3 (pink solid symbols).

field of EuS is much higher than the observed coercive field [Fig. 1(f)], as already observed in films of EuS deposited at room temperature [20,59]. In contrast to the SMR, both SSE curves [Figs. 4(b) and 4(c)] reach a maximum at $\mu_0 H \approx 0.5$ T, followed by a gradual reduction of the SSE amplitude for higher magnetic fields. Such a decay is characteristic of SSE-induced voltages, for which the opening of the Zeeman gap affects the magnon population. According to the SSE theory, when the Zeeman energy $g\mu_B H$ is larger than the thermal energy $k_B T$, magnons cannot be thermally excited, leading to the suppression of the local SSE, where g, μ_B, and k_B are the g factor, Bohr magneton, and Boltzmann constant, respectively [60–62]. More interestingly, we note that the local SSE signal suppression at the maximum applied field ($\mu_0 H = 9$ T) is almost 50% of the maximum signal whereas nonlocal SSE signal suppression reaches 80%, as is shown in Fig. 4(d). Such a difference can be accounted for by the distinct way magnon currents reach the EuS/Pt interface in the local and nonlocal case. In fact, the magnon induced nonlocal voltage should decay exponentially on the scale of the magnon diffusion length, in contrast to the local voltage case. Therefore, as the magnon diffusion length is also suppressed as the magnetic field is increased, a stronger suppression of the signal should be expected for the nonlocal case [63].

D. Magnon diffusion length

Finally, we study the dependence of the nonlocal SSE amplitude on the injector-detector distance d, to unravel the mechanism by which the magnon currents propagate through the EuS medium. As shown in Fig. 5, the data can be fitted with an exponential decay law, characteristic of thermally generated magnons in the relaxation regime [4,64]. Moreover, we note that the data could not be fitted by power laws, indicating that the signal is not driven by the radial decay of a thermal gradient through the sample, but by the redistribution of the magnon population (see Supplemental Material [43], Sec. S4). From the exponential fit, we extract a magnon diffusion length $\ell_m^{th} = 140 \pm 30$ nm at 2 K and 0.3 T. This value is of the same order as the one reported by Gao *et al.* in the ferrimagnet TmIG, where a 15-nm-thick film results in $\ell_m^{th} = 300$ nm at 0.5 T and room temperature [65]. In comparison to the best YIG samples, where $\ell_m^{th} \sim 7$ μm at low temperatures in a 210-nm-thick film and the electrical magnon diffusion length $\ell_m^{e} \sim 3$ μm in 10−15-nm-thick films [6,54], the EuS value is more than one order of magnitude smaller. However, we note here that several studies in YIG films reported ℓ_m^{th} values at room temperature comparable with the ℓ_m^{th} value that we observe in EuS [66–69]. At this point, it is important to consider the Gilbert damping (α_G), since it is linked to the magnon diffusion length. Reducing

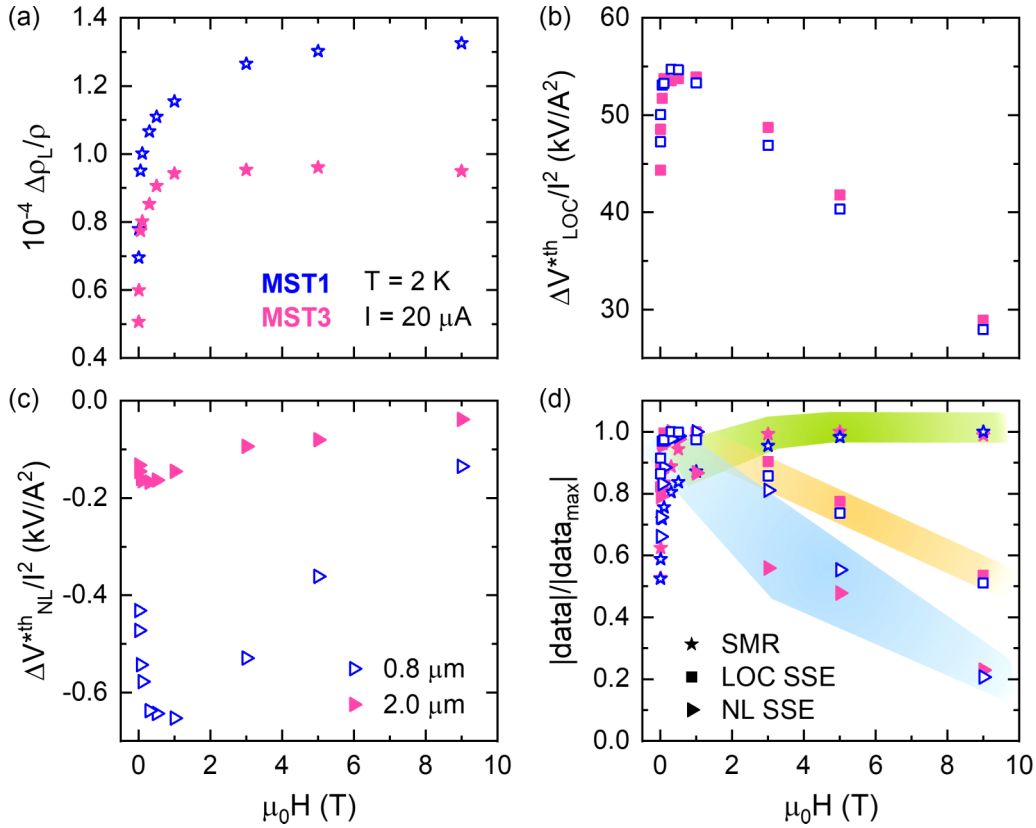

FIG. 4. (a) SMR, (b) local SSE, and (c) nonlocal SSE amplitudes (as defined in Fig. 2) as a function of the magnetic field at $T = 2$ K and $I = 20\,\mu$A. (d) Comparison of SMR, local SSE, and nonlocal SSE amplitudes normalized to their maximum values. Colored shadows are a guide to the eye, being green for the SMR amplitudes, orange for the local amplitudes and blue for the nonlocal amplitudes. Data correspond to devices MST1 (blue open symbols) and MST3 (pink solid symbols).

α_G implies increasing the magnon spin-relaxation time and, therefore, the magnon diffusion length [2,37]. To verify this relationship, we performed FMR measurements in the very same sample where the measured devices are located. Our results in the EuS thin film yields $\alpha_G^{EuS} = 4 \times 10^{-2}$ at 2 K (see the Supplemental Material [43], Sec. S5), which is two orders of magnitude higher than the case of YIG thin films measured at room temperature ($\alpha_G^{YIG} \sim 10^{-4}$) [4,6], in agreement with the difference observed in the magnon diffusion length.

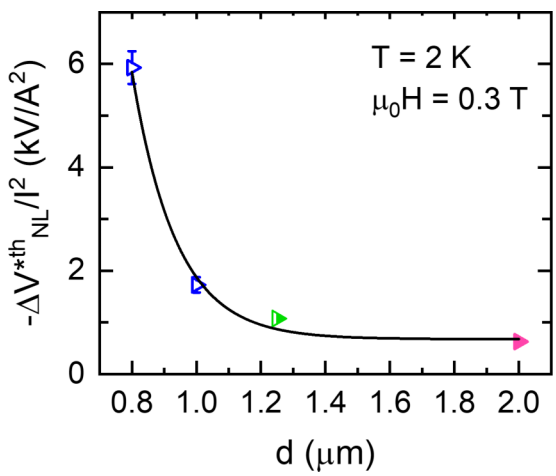

FIG. 5. Amplitude of the nonlocal SSE as a function of injector-detector separation distance measured at $T = 2$ K, $\mu_0 H = 0.3$ T, and $I = 4\,\mu$A. Black solid line is a fit to an exponential decay.

IV. CONCLUSIONS

To summarize, we demonstrated the transport of incoherent magnon currents in polycrystalline films of EuS. Below T_C, we observe a thermally induced response in both local and nonlocal transport measurements. Considering the angular, temperature, and magnetic field dependence of such signals, we ascribe the measured thermal voltages to the SSE. By studying the length dependence of the nonlocal transport signal, we extract a magnon diffusion length of $\ell_m^{th} = 140 \pm 30$ nm at 2 K and 0.3 T. This value, short compared to other studied materials such as YIG, correlates well with an enhanced Gilbert damping caused by the polycrystalline structure of the studied EuS films. While we expect that a significantly smaller Gilbert damping in epitaxial EuS films could lead to an improvement of the magnon diffusion length, we highlight the observation of magnon currents propagating even through a polycrystalline ferromagnetic insulator film, as compared to the case of YIG films. Despite the relatively short ℓ_m^{th} observed, our work shows that the transport of spin currents by incoherent magnons through EuS films should be taken into account when studying EuS-based heterostructures. As for perspectives, our results evidence the opportunity

of studying the interaction between magnon currents and superconductivity in systems comprising, for example, superconductor/EuS interfaces, following recent experimental and theoretical works [70,71]. Moreover, as sizeable thermoelectric effects may occur in spin-split superconductors, such as Al/EuS bilayers, the role of the observed SSE could be further explored in such a context [72–75].

ACKNOWLEDGMENTS

We would like to thank M. Ipatov for technical expertise in the FMR measurements. We acknowledge funding by the Spanish MCIN/AEI/ 10.13039/501100011033 and by ERDF A way of making Europe (Projects No. PID2021-122511OB-I00, No. PID2020-114252GB-I00, No. TED2021-130292B-C42, and Maria de Maeztu Units of Excellence Programme No. CEX2020-001038-M), by the Basque Government (Project No. IT1591-22), by the Gipuzkoa Quantum Programme (Project No. QUAN 36/2022) and by the European Union H2020 Programme (Projects No. 965046-INTERFAST and No. 964396-SINFONIA). M.X.A.-P. thanks the Spanish MCIN/AEI for a Ph.D. fellowship (Grant No. PRE-2019-089833). S.C. acknowledges support from the European Commission for a Marie Sklodowska-Curie individual fellowship (Grant No. 796817-ARTEMIS). W.S. acknowledges financial support from Polish National Agency for Academic Exchange (Grant No. PPN/BEK/2020/1/00118/DEC/1). M.G. acknowledges support from the Ramon y Cajal Programme by the Spanish MCIN/AEI (Grant No. RYC2021-031705-I).

[1] A. Brataas, B. van Wees, O. Klein, G. de Loubens, and M. Viret, Spin insulatronics, Phys. Rep. **885**, 1 (2020).

[2] M. Althammer, All-electrical magnon transport experiments in magnetically ordered insulators, Phys. Status Solidi RRL **15**, 2100130 (2021).

[3] M. Althammer, Pure spin currents in magnetically ordered insulator/normal metal heterostructures, J. Phys. D: Appl. Phys. **51**, 313001 (2018).

[4] L. J. Cornelissen, J. Liu, R. A. Duine, J. Ben Youssef, and B. J. van Wees, Long-distance transport of magnon spin information in a magnetic insulator at room temperature, Nat. Phys. **11**, 1022 (2015).

[5] J. Shan, P. Bougiatioti, L. Liang, G. Reiss, T. Kuschel, and B. J. van Wees, Nonlocal magnon spin transport in $NiFe_2O_4$ thin films, Appl. Phys. Lett. **110**, 132406 (2017).

[6] X.-Y. Wei, O. A. Santos, C. H. S. Lusero, G. E. W. Bauer, J. Ben Youssef, and B. J. van Wees, Giant magnon spin conductivity in ultrathin yttrium iron garnet films, Nat. Mater. **21**, 1352 (2022).

[7] R. Lebrun, A. Ross, S. A. Bender, A. Qaiumzadeh, L. Baldrati, J. Cramer, A. Brataas, R. A. Duine, and M. Kläui, Tunable long-distance spin transport in a crystalline antiferromagnetic iron oxide, Nature (London) **561**, 222 (2018).

[8] P. Muduli, R. Schlitz, T. Kosub, R. Hübner, A. Erbe, D. Makarov, and S. T. B. Goennenwein, Local and nonlocal spin Seebeck effect in lateral Pt-Cr_2O_3-Pt devices at low temperatures, APL Mater. **9**, 021122 (2021).

[9] N. Ito, T. Kikkawa, J. Barker, D. Hirobe, Y. Shiomi, and E. Saitoh, Spin Seebeck effect in the layered ferromagnetic insulators $CrSiTe_3$ and $CrGeTe_3$, Phys. Rev. B **100**, 060402(R) (2019).

[10] W. Xing, L. Qiu, X. Wang, Y. Yao, Y. Ma, R. Cai, S. Jia, X. C. Xie, and W. Han, Magnon transport in quasi-two-dimensional van der Waals antiferromagnets, Phys. Rev. X **9**, 011026 (2019).

[11] S. Qi, D. Chen, K. Chen, J. Liu, G. Chen, B. Luo, H. Cui, L. Jia, J. Li, M. Huang *et al.*, Giant electrically tunable magnon transport anisotropy in a van der Waals antiferromagnetic insulator, Nat. Commun. **14**, 2526 (2023).

[12] D. K. de Wal, A. Iwens, T. Liu, P. Tang, G. E. W. Bauer, and B. J. van Wees, Long-distance magnon transport in the van der Waals antiferromagnet $CrPS_4$, Phys. Rev. B **107**, L180403 (2023).

[13] K. Mallick, A. A. Wagh, A. Ionescu, C. H. W. Barnes, and P. S. Anil Kumar, Magnetoresistance effects in Pt/EuO_{1-x}, Appl. Phys. Lett. **116**, 202405 (2020).

[14] P. Rosenberger, M. Opel, S. Geprägs, H. Huebl, R. Gross, M. Müller, and M. Althammer, Quantifying the spin mixing conductance of EuO/W heterostructures by spin Hall magnetoresistance experiments, Appl. Phys. Lett. **118**, 192401 (2021).

[15] J. M. Gomez-Perez, X. P. Zhang, F. Cavalle, M. Ilyn, C. González-Orellana, M. Gobbi, C. Rogero, A. Chuvilin, V. N. Golovach, L. E. Hueso *et al.*, Strong interfacial exchange field in a heavy metal/ferromagnetic insulator system determined by spin Hall magnetoresistance, Nano Lett. **20**, 6815 (2020).

[16] T. R. McGuire, B. E. Argyle, M. W. Shafer, and J. S. Smart, Magnetic properties of some divalent europium compounds, J. Appl. Phys. **34**, 1345 (1963).

[17] L. Passell, O. W. Dietrich, and J. Als-Nielsen, Neutron scattering from the Heisenberg ferromagnets EuO and EuS. I. The exchange interactions, Phys. Rev. B **14**, 4897 (1976).

[18] K. Y. Ahn, M. W. Shafer, and T. J. Watson, Preparation and properties of EuS films and effects of Fe doping, IEEE Trans. Magn. **7**, 394 (1971).

[19] P. Wei, S. Lee, F. Lemaitre, L. Pinel, D. Cutaia, W. Cha, F. Katmis, Y. Zhu, D. Heiman, J. Hone *et al.*, Strong interfacial exchange field in the graphene/EuS heterostructure, Nat. Mater. **15**, 711 (2016).

[20] A. Hijano, S. Ilić, M. Rouco, C. González-Orellana, M. Ilyn, C. Rogero, P. Virtanen, T. T. Heikkilä, S. Khorshidian, M. Spies *et al.*, Coexistence of superconductivity and spin-splitting fields in superconductor/ferromagnetic insulator bilayers of arbitrary thickness, Phys. Rev. Res. **3**, 023131 (2021).

[21] J. S. Moodera, X. Hao, G. A. Gibson, and R. Meservey, Electron-spin polarization in tunnel junctions in zero applied field with ferromagnetic EuS barriers, Phys. Rev. Lett. **61**, 637 (1988).

[22] X. Hao, J. S. Moodera, and R. Meservey, Spin-filter effect of ferromagnetic europium sulfide tunnel barriers, Phys. Rev. B **42**, 8235 (1990).

[23] E. Strambini, M. Spies, N. Ligato, S. Ilić, M. Rouco, C. González-Orellana, M. Ilyn, C. Rogero, F. S. Bergeret, J. S. Moodera *et al.*, Superconducting spintronic tunnel diode, Nat. Commun. **13**, 2431 (2022).

[24] Y. Liu, S. Vaitiekėnas, S. Martí-Sánchez, C. Koch, S. Hart, Z. Cui, T. Kanne, S. A. Khan, R. Tanta, S. Upadhyay *et al.*, Semiconductor-ferromagnetic insulator-superconductor nanowires: Stray field and exchange field, Nano Lett. **20**, 456 (2020).

[25] G. De Simoni, E. Strambini, J. S. Moodera, F. S. Bergeret, and F. Giazotto, Toward the absolute spin-valve effect in superconducting tunnel junctions, Nano Lett. **18**, 6369 (2018).

[26] S. Diesch, P. Machon, M. Wolz, C. Sürgers, D. Beckmann, W. Belzig, and E. Scheer, Creation of equal-spin triplet superconductivity at the Al/EuS interface, Nat. Commun. **9**, 5248 (2018).

[27] E. Strambini, V. N. Golovach, G. De Simoni, J. S. Moodera, F. S. Bergeret, and F. Giazotto, Revealing the magnetic proximity effect in EuS/Al bilayers through superconducting tunneling spectroscopy, Phys. Rev. Mater. **1**, 054402 (2017).

[28] S. Vaitiekėnas, Y. Liu, P. Krogstrup, and C. M. Marcus, Zero-bias peaks at zero magnetic field in ferromagnetic hybrid nanowires, Nat. Phys. **17**, 43 (2021).

[29] Y. liu, A. Luchini, S. Martí-Sánchez, C. Koch, S. Schuwalow, S. A. Khan, T. Stankevič, S. Francoual, J. R. L. Mardegan, J. A. Krieger *et al.*, Coherent epitaxial semiconductor-ferromagnetic insulator InAs/EuS interfaces: Band alignment and magnetic structure, ACS Appl. Mater. Interfaces **12**, 8780 (2020).

[30] Z. Geng, A. Hijano, S. Ilic, M. Ilyn, I. J. Maasilta, A. Monfardini, M. Spies, E. Strambini, P. Virtanen, M. Calvo *et al.*, Superconductor-ferromagnet hybrids for non-reciprocal electronics and detectors, Supercond. Sci. Technol. **36**, 123001 (2023).

[31] E. Sagasta, Y. Omori, M. Isasa, M. Gradhand, L. E. Hueso, Y. Niimi, Y. C. Otani, and F. Casanova, Tuning the spin Hall effect of Pt from the moderately dirty to the superclean regime, Phys. Rev. B **94**, 060412(R) (2016).

[32] J. M. Gómez Pérez, Spin Transport in Magnetic Insulator/Heavy Metal Heterostructures, Ph.D. thesis, CIC nanoGUNE-UPV/EHU, 2020, https://www.nanogune.eu/en/publications/phd-theses/134.

[33] F. Casanova, A. Sharoni, M. Erekhinsky, and I. K. Schuller, Control of spin injection by direct current in lateral spin valves, Phys. Rev. B **79**, 184415 (2009).

[34] M. Schreier, N. Roschewsky, E. Dobler, S. Meyer, H. Huebl, R. Gross, and S. T. B. Goennenwein, Current heating induced spin Seebeck effect, Appl. Phys. Lett. **103**, 242404 (2013).

[35] J. M. Gomez-Perez, S. Vélez, L. E. Hueso, and F. Casanova, Differences in the magnon diffusion length for electrically and thermally driven magnon currents in $Y_3Fe_5O_{12}$, Phys. Rev. B **101**, 184420 (2020).

[36] P. Pirro, V. I. Vasyuchka, A. A. Serga, and B. Hillebrands, Advances in coherent magnonics, Nat. Rev. Mater. **6**, 1114 (2021).

[37] L. J. Cornelissen, K. J. H. Peters, G. E. W. Bauer, R. A. Duine, and B. J. van Wees, Magnon spin transport driven by the magnon chemical potential in a magnetic insulator, Phys. Rev. B **94**, 014412 (2016).

[38] H. Nakayama, M. Althammer, Y. T. Chen, K. Uchida, Y. Kajiwara, D. Kikuchi, T. Ohtani, S. Geprägs, M. Opel, S. Takahashi *et al.*, Spin Hall magnetoresistance induced by a nonequilibrium proximity effect, Phys. Rev. Lett. **110**, 206601 (2013).

[39] Y. T. Chen, S. Takahashi, H. Nakayama, M. Althammer, S. T. B. Goennenwein, E. Saitoh, and G. E. W. Bauer, Theory of spin Hall magnetoresistance, Phys. Rev. B **87**, 144411 (2013).

[40] K. I. Uchida, Transport phenomena in spin caloritronics, Proc. Jpn. Acad. Ser. B: Phys. Biol. Sci. **97**, 69 (2020).

[41] H. Adachi, K. I. Uchida, E. Saitoh, and S. Maekawa, Theory of the spin Seebeck effect, Rep. Prog. Phys. **76**, 036501 (2013).

[42] M. Isasa, A. Bedoya-Pinto, S. Vélez, F. Golmar, F. Sánchez, L. E. Hueso, J. Fontcuberta, and F. Casanova, Spin Hall magnetoresistance at $Pt/CoFe_2O_4$ interfaces and texture effects, Appl. Phys. Lett. **105**, 142402 (2014).

[43] See Supplemental Material at http://link.aps.org/supplemental/10.1103/PhysRevB.108.224420 for additional longitudinal magnetoresistance measurements, current-dependent measurements, electrical and thermal excitation of magnons, magnetization measurements, and ferromagnetic resonance measurements. It also includes Refs. [44–46].

[44] P. K. Muduli, M. Kimata, Y. Omori, T. Wakamura, S. P. Dash, and Y. C. Otani, Detection of the interfacial exchange field at a ferromagnetic insulator-nonmagnetic metal interface with pure spin currents, Phys. Rev. B **98**, 024416 (2018).

[45] S. Azzawi, A. T. Hindmarch, and D. Atkinson, Magnetic damping phenomena in ferromagnetic thin-films and multilayers, J. Phys. D: Appl. Phys. **50**, 473001 (2017).

[46] C. Bilzer, T. Devolder, J. Von Kim, G. Counil, C. Chappert, S. Cardoso, and P. P. Freitas, Study of the dynamic magnetic properties of soft CoFeB films, J. Appl. Phys. **100**, 053903 (2006).

[47] S. Vélez, A. Bedoya-Pinto, W. Yan, L. E. Hueso, and F. Casanova, Competing effects at Pt/YIG interfaces: Spin Hall magnetoresistance, magnon excitations, and magnetic frustration, Phys. Rev. B **94**, 174405 (2016).

[48] M. Althammer, S. Meyer, H. Nakayama, M. Schreier, S. Altmannshofer, M. Weiler, H. Huebl, S. Geprägs, M. Opel, R. Gross *et al.*, Quantitative study of the spin Hall magnetoresistance in ferromagnetic insulator/normal metal hybrids, Phys. Rev. B **87**, 224401 (2013).

[49] M. Weiler, M. Althammer, M. Schreier, J. Lotze, M. Pernpeintner, S. Meyer, H. Huebl, R. Gross, A. Kamra, J. Xiao *et al.*, Experimental test of the spin mixing interface conductivity concept, Phys. Rev. Lett. **111**, 176601 (2013).

[50] R. Schlitz, S. Vélez, A. Kamra, C. H. Lambert, M. Lammel, S. T. B. Goennenwein, and P. Gambardella, Control of nonlocal magnon spin transport via magnon drift currents, Phys. Rev. Lett. **126**, 257201 (2021).

[51] K. Ganzhorn, T. Wimmer, J. Cramer, R. Schlitz, S. Geprägs, G. Jakob, R. Gross, H. Huebl, M. Kläui, and S. T. B. Goennenwein, Temperature dependence of the non-local spin Seebeck effect in YIG/Pt nanostructures, AIP Adv. **7**, 085102 (2017).

[52] J. Shan, L. J. Cornelissen, N. Vlietstra, J. ben Youssef, T. Kuschel, R. A. Duine, and B. J. van Wees, Influence of yttrium iron garnet thickness and heater opacity on the nonlocal transport of electrically and thermally excited magnons, Phys. Rev. B **94**, 174437 (2016).

[53] X. J. Zhou, G. Y. Shi, J. H. Han, Q. H. Yang, Y. H. Rao, H. W. Zhang, L. L. Lang, S. M. Zhou, F. Pan, and C. Song, Lateral transport properties of thermally excited magnons in yttrium iron garnet films, Appl. Phys. Lett. **110**, 062407 (2017).

[54] L. J. Cornelissen, J. Shan, and B. J. van Wees, Temperature dependence of the magnon spin diffusion length and magnon spin conductivity in the magnetic insulator yttrium iron garnet, Phys. Rev. B **94**, 180402(R) (2016).

[55] S. T. B. Goennenwein, R. Schlitz, M. Pernpeintner, K. Ganzhorn, M. Althammer, R. Gross, and H. Huebl, Non-local magnetoresistance in YIG/Pt nanostructures, Appl. Phys. Lett. **107**, 172405 (2015).

[56] K. Oyanagi, J. M. Gómez-Pérez, X. P. Zhang, T. Kikkawa, Y. Chen, E. Sagasta, A. Chuvilin, L. E. Hueso, V. N. Golovach, F. S. Bergeret *et al.*, Paramagnetic spin Hall magnetoresistance, Phys. Rev. B **104**, 134428 (2021).

[57] X. P. Zhang, F. S. Bergeret, and V. N. Golovach, Theory of spin Hall magnetoresistance from a microscopic perspective, Nano Lett. **19**, 6330 (2019).

[58] H. Adachi, Y. Yamamoto, and M. Ichioka, Spin Seebeck effect in a simple ferromagnet near T_c: A Ginzburg-Landau approach, J. Phys. D: Appl. Phys. **51**, 144001 (2018).

[59] G. X. Miao and J. S. Moodera, Controlling magnetic switching properties of EuS for constructing double spin filter magnetic tunnel junctions, Appl. Phys. Lett. **94**, 182504 (2009).

[60] T. Kikkawa, K. I. Uchida, S. Daimon, Z. Qiu, Y. Shiomi, and E. Saitoh, Critical suppression of spin Seebeck effect by magnetic fields, Phys. Rev. B **92**, 064413 (2015).

[61] K. Oyanagi, T. Kikkawa, and E. Saitoh, Magnetic field dependence of the nonlocal spin Seebeck effect in Pt/YIG/Pt systems at low temperatures, AIP Adv. **10**, 015031 (2020).

[62] T. Kikkawa, K. I. Uchida, S. Daimon, and E. Saitoh, Complete suppression of longitudinal spin Seebeck effect by frozen magnetization dynamics in $Y_3Fe_5O_{12}$, J. Phys. Soc. Jpn. **85**, 065003 (2016).

[63] L. J. Cornelissen and B. J. van Wees, Magnetic field dependence of the magnon spin diffusion length in the magnetic insulator yttrium iron garnet, Phys. Rev. B **93**, 020403(R) (2016).

[64] J. Shan, L. J. Cornelissen, J. Liu, J. Ben Youssef, L. Liang, and B. J. van Wees, Criteria for accurate determination of the magnon relaxation length from the nonlocal spin Seebeck effect, Phys. Rev. B **96**, 184427 (2017).

[65] J. Gao, C. H. Lambert, R. Schlitz, M. Fiebig, P. Gambardella, and S. Vélez, Magnon transport and thermoelectric effects in ultrathin $Tm_3Fe_5O_{12}$/Pt nonlocal devices, Phys. Rev. Res. **4**, 043214 (2022).

[66] T. B. Noack, H. Y. Musiienko-Shmarova, T. Langner, F. Heussner, V. Lauer, B. Heinz, D. A. Bozhko, V. I. Vasyunchka, A. Pomyalov, V. S. L'vov *et al.*, Spin Seebeck effect and ballistic transport of quasi-acoustic magnons in room-temperature yttrium iron garnet films, J. Phys. D: Appl. Phys. **51**, 234003 (2018).

[67] E. Chavez-Angel, R. A. Zarate, S. Fuentes, E. J. Guo, M. Kläui, and G. Jakob, Reconstruction of an effective magnon mean free path distribution from spin Seebeck measurements in thin films, New J. Phys. **19**, 013011 (2017).

[68] A. Kehlberger, U. Ritzmann, D. Hinzke, E. J. Guo, J. Cramer, G. Jakob, M. C. Onbasli, D. H. Kim, C. A. Ross, M. B. Jungfleisch *et al.*, Length scale of the spin Seebeck effect, Phys. Rev. Lett. **115**, 096602 (2015).

[69] U. Ritzmann, D. Hinzke, and U. Nowak, Propagation of thermally induced magnonic spin currents, Phys. Rev. B **89**, 024409 (2014).

[70] K. R. Jeon, J. C. Jeon, X. Zhou, A. Migliorini, J. Yoon, and S. S. P. Parkin, Giant transition-state quasiparticle spin-Hall effect in an exchange-spin-split superconductor detected by nonlocal magnon spin transport, ACS Nano **14**, 15874 (2020).

[71] L. G. Johnsen, H. T. Simensen, A. Brataas, and J. Linder, Magnon spin current induced by triplet cooper pair supercurrents, Phys. Rev. Lett. **127**, 207001 (2021).

[72] F. Giazotto and F. S. Bergeret, Very large thermal rectification in ferromagnetic insulator-based superconducting tunnel junctions, Appl. Phys. Lett. **116**, 192601 (2020).

[73] F. Giazotto, P. Solinas, A. Braggio, and F. S. Bergeret, Ferromagnetic-insulator-based superconducting junctions as sensitive electron thermometers, Phys. Rev. Appl. **4**, 044016 (2015).

[74] Z. Geng, A. P. Helenius, T. T. Heikkilä, and I. J. Maasilta, Superconductor-ferromagnet tunnel junction thermoelectric bolometer and calorimeter with a SQUID readout, J. Low Temp. Phys. **199**, 585 (2020).

[75] P. Machon, M. Eschrig, and W. Belzig, Giant thermoelectric effects in a proximity-coupled superconductor-ferromagnet device, New J. Phys. **16**, 073002 (2014).